Local investigations on the gas-liquid mass transfer around Taylor bubbles flowing in a meandering millimetric square channel

Lixia Yang, Karine Loubiere, Nicolas Dietrich, Claude Le Men, Christophe Gourdon, Gilles Hébrard

Local investigations on the gas-liquid mass transfer around Taylor bubbles flowing in a meandering millimetric square channel

Lixia Yang [a,b], Karine Loubière [b,*], Nicolas Dietrich [a], Claude Le Men [a], Christophe Gourdon [b], Gilles Hébrard [a]

[a] Laboratoire d'Ingénierie des Systèmes Biologiques et des Procédés (LISBP), Université de Toulouse, CNRS, INRA, INSA, Toulouse, France
[b] Laboratoire de Génie Chimique, Université de Toulouse, CNRS, INPT, UPS, Toulouse, France

ARTICLE INFO

Keywords:
Gas-liquid mass transfer
Taylor bubbles
Meandering channel
Colorimetric technique
Image processing

ABSTRACT

Gas-liquid mass transfer around Taylor bubbles moving in a meandering millimetric square channel was locally visualized and characterized in the present study. For that, the colorimetric technique proposed by Dietrich et al. (2013) was implemented. With this technique, the evolution of equivalent oxygen concentration fields in the liquid slugs passing through one and several bends was firstly described. In particular, it was observed how the flow structure (recirculation zones) inside the liquid slugs were twisted and split by the periodic bends (centrifugal effect), until reaching, after several bends, a uniform O_2 concentration inside the liquid slugs. The influence of the "turning point", joining two "straight" sections of meandering channel was also highlighted: a slowing down of the gas-liquid mass transfer was clearly shown. Volumetric mass transfer coefficients were determined at last by fitting the experimental axial profiles of averaged oxygen concentrations in the liquid slugs (before the turning point) with the ones predicted by a classical plug-flow model.

1. Introduction

Since the last decade, process intensification opens up interesting perspectives for the fine chemical and pharmaceutical industries (Stankiewicz and Moulijn, 2000; Tochon et al., 2010; Commenge and Falk, 2014; Gourdon et al., 2015). A wide range of chemistries has been investigated through the implementation of flow reactors, showing the advantages and the improvements related to such technologies, with regards to quality, safety, competitiveness and eco-impact (Pelleter and Renaud, 2009; Nieves-Remacha et al., 2013; Darvas et al., 2014; Elgue et al., 2015). In this way, various equipments have been developed, benefiting from miniaturization techniques and micro (or milli) fluidics. Most of them are the devices where chemical reactions are performed in narrow channels involving a very high surface area to volume ratio and thus providing very efficient rates of mass and heat transfer.

Among all the process intensification technologies, heat exchanger reactors (HEX reactors), combining a reactor and a heat exchanger in only one unit, are particularly performing in terms of versatility and modularity features, but also of heat and mass transfer capabilities (Anxionnaz et al., 2008; Anxionnaz, 2009; Théron et al., 2014). They now become standard tools for process development and continuous production. In order to combine intensified heat and mass transfers, high residence time and compactness in such HEX reactors, the use of 2D-structured meandering (or tortuous or serpentine or wavy) channel structures constitutes an interesting solution. Indeed, contrary to the case in a straight channel, the occurrence of curvatures (or bends) generates flow instabilities and secondary flows (Dean vortices) in fluid motion (Dean, 1928), where the mixing between the core fluid and near-wall fluid can be improved; the boundary layers are also disrupted and thinned, thus affecting positively heat and mass

* Corresponding author.
E-mail address: karine.loubiere@ensiacet.fr (K. Loubière).

http://dx.doi.org/10.1016/j.ces.2017.03.007

Nomenclature

a	the interfacial area, m^{-1}
A	l^2, cross-sectional area of the channel, m^2
C	equivalent oxygen concentration, kg m^{-3}
C	average equivalent oxygen concentration in the liquid slug of the unit cell, kg m^{-3}
C^*	dissolved oxygen concentration at saturation, kg m^{-3}
C_0	distribution parameter
d_h	hydraulic diameter of the meandering channel, m
e	eccentricity, $e^2 = 1 - l^2/L_B{}^2$
j	superficial velocity, m s^{-1}
k_L	the liquid side mass transfer coefficient, m s^{-1}
k_La	volumetric mass transfer coefficient, s^{-1}
l	width of the channel, m
L	length, m
Q	flow rate, m^3 s^{-1}
t	flowing time, s
U	velocity, m s^{-1}
V	volume, m^3
X	axial position, m
β	volumetric quality of gas
ε	gas hold-up
φ	volumetric mass flux of the transferred O_2 per unit of bubble surface, kg m^2 s^{-1}

Greek letters

μ_L	dynamic viscosity of the dye solution, Pa s
ρ_L	density of the dye solution, kg m^{-3}
σ_L	surface tension of the dye solution, N m^{-1}

Dimensionless numbers

Ca	Capillary number, $=\mu_L \times U_B/\sigma_L$, dimensionless
Ce	Centrifugal number, $=\rho_L \times U_B{}^2 \times l^2/\sigma_L \times r_c$, dimensionless
Re	Reynold number, $=\rho_L \times U_B \times l/\mu_L$, dimensionless
We	Weber number, $=\rho_L \times U_B{}^2 \times l/\sigma_L$, dimensionless

Subscripts

B	bubble
bt	before turning point
d	drift velocity
G	gas phase
L	liquid phase
s	liquid slug
UC	unit cell

transfer phenomena. Most of the existed literature dealing with such type of meandering channels focus on the study of single liquid phase flows, reactive or not (Xiong and Chung, 2007; Anxionnaz-Minvielle et al., 2013; Karale et al., 2013; Dai et al., 2015a). Few attention has been surprisingly paid on the implementation of gas-liquid systems in meandering channels, whereas: (i) the gas-liquid systems occupy a key place in scientific research and industrial application fields (hydrogenations, sensitized photo-oxygenations, fluorinations, biochemical reactions); (ii) there still raises many fundamental questions (coupling between transport phenomena and kinetics); (iii) studies in straight micro- or millimetric channels are the object of an abundant literature (van Baten and Krishna, 2004; Roudet et al., 2011; Yao et al., 2014; Haghnegahdar et al., 2016; Haase et al., 2016; Butler et al., 2016). In such two-phase reactive systems, the knowledge of mass transfer between gas and liquid phases is then extremely important; as managing the chemical kinetics, it can become the limiting step controlling the chemical reactions in terms of conversion and selectivity.

While the influence of the occurrence of bends in millimetric channels on the gas-liquid hydrodynamics (i.e. flow regime, mixing efficiency, interfacial area) has been highlighted by several authors (Günther et al., 2004; Fries and von Rohr, 2009; Dessimoz et al., 2010), rare are at present the studies quantifying how curvatures affect the gas-liquid mass transfer (Roudet et al., 2011; Kuhn and Jensen, 2012). Roudet et al. (2011) showed that, when compared to a straight channel of identical compactness and sectional-area, the meandering channel induced: (i) a delay in the transition from Taylor to annular-slug regimes; (ii) a rise of 10–20% in bubble lengths while conserving almost identical slug lengths; (iii) higher deformations of bubble nose and rear due to centrifugal forces (bends). They also observed that, for the Taylor flow regime, k_La increased coherently when increasing superficial gas velocity j_g, and that the meandering geometry had a small influence. On the contrary, this effect was found no more negligible for the slug-annular flow regime. At last, they demonstrated that, at identical compactness, the meandering channel was found to be the most competitive. As these authors used a global experimental method (measurements of concentrations in dissolved oxygen along the channel length by oxygen microsensors), the full understanding of the mechanism controlling the gas-liquid mass transfer in a meandering channel could not be achieved, and in particular the contribution of the curvatures. In order to fill these gaps, local measurements, such as concentration fields of the transferred gas phase around bubbles in the liquid slugs and films, are required. However, to our best knowledge, there exists no research on the local visualization and characterization of gas-liquid mass transfer in meandering channels.

With regard to this context, this paper aims at locally studying the mass transfer around Taylor bubbles flowing in a meandering millimetric square channel, identical in elementary shape to the one used by Roudet et al. (2011) but longer. For this purpose, the colorimetric technique proposed by Dietrich et al. (2013) will be used, consisting in implementing a redox reaction involving an oxygen-sensitive dye (resazurin). Its relevancy for locally visualizing and characterizing gas-liquid mass transfer at different scales has been outlined by Kherbeche et al. (2013) and Yang et al. (2016b). In addition, the conditions required to avoid any enhancement of the gas-liquid mass transfer by this reaction have been recently identified (Yang et al., 2016a); for that, the Hatta number and enhancement factor have been quantified from the determination of the characteristic time of the redox reaction kinetic and of the diffusion coefficients of the dye and of oxygen in the reactive medium. In comparison with PLIF technique (e.g. Butler et al., 2016), the colorimetric method is more convenient and user friendly as it does not need any laser excitation or inserting a physical sensor.

This paper will be structured as follows. The hydrodynamics of gas-liquid system (air/reactive medium) will be firstly characterized, in particular in terms of the gas-liquid flow map, overall gas hold-up, bubble length, shape and velocity. The colorimetric technique will be implemented in a second time, only in the case of the Taylor regime. The fields of equivalent oxygen concentration in the liquid slugs will be presented and discussed, as well as their changes according to the locations in the bend and all along the channel length; the influence of gas and liquid flow rates on these

fields will be also outlined. From them, the evolution of averaged O_2 concentration with the axial location in the channel will be determined, enabling the overall volumetric mass transfer coefficients to be deduced using the classical plug-flow model. At last, these data will make possible the calculation of liquid-side mass transfer coefficients, based on an accurate determination of interfacial areas.

2. Materials and methods

2.1. General principles of the colorimetric technique

The colorimetric technique, proposed by Dietrich et al. (2013), is based on an oxygen-sensitive dye, named resazurin, that could react with oxygen in the presence of sodium hydroxide (NaOH) and glucose solution. In the reduced form, named dihydroresorufin, the solution is colorless, while in presence of oxygen, the oxidized form, named resorufin, is characterized by an intense pink color. As shown by previous works (Dietrich et al., 2013; Kherbeche et al., 2013; Yang et al., 2016b), the main advantage of this technique is that the extent of the oxidation reaction which corresponds to the amount of transferred (or dissolved) oxygen, are directly proportional to the color intensity (grey value) under a given concentration of resazurin. For each system, an optimal composition of the reactional medium should be determined, by taking into account: (i) the balance between the quasi-instantaneous oxidation and the slow reverse reduction kinetics; (ii) the requirements in terms of adequate color intensity levels; (iii) the fact that no enhancement of the gas-liquid mass transfer by the reaction should exist. In the present case, this led to sodium hydroxide and glucose solutions both diluted at 20 g L^{-1} in deionized water, and to a concentration of resazurin fixed at 0.1 g L^{-1}; according to Yang et al. (2016a), the corresponding enhancement factor E equals to 1.03.

2.2. Fluid properties

All the experiments were performed at 293.15 K and atmospheric pressure. For the hydrodynamic experiments, the liquid phase was dye-free, composed only of D-glucose anhydrous (Fischer Scientific®, CAS 50-99-7) and sodium hydroxide (VWR®, CAS 1310-73-2), both diluted at 20 g L^{-1} in deionized water (conductivity: 51.2 μS m^{-1}). For the mass transfer experiments, resazurin (Sigma Aldrich®, CAS 62758-13-8, molecular mass: 229.19 g mol^{-1}) which concentration was fixed at 0.1 g L^{-1}, was added to the previous solution. The density ρ_L, dynamic viscosity μ_L and static surface tension σ_L were measured by means of a pycnometer ($\rho_L \pm 0.2$ kg m^{-3}), a RM180 Rheomat Rheometric Scientific® viscometer ($\mu_L \pm 10^{-3}$ mPa s), and a Digidrop GBX® or Krüss tensiometer ($\sigma_L \pm 0.5$ mN m^{-1}) respectively. The oxygen saturation concentration $C^*_{O_2}$ was measured by implementing the Winkler technique (Winkler, 1888) and by means of optical oxygen probes (Hach-Lange®), and found equal to 8.15 mg L^{-1}. All the physico-chemical properties are reported in Table 1.

2.3. Description of the experimental set-up

The experimental set-up was depicted in Fig. 1(a). It consisted of a meandering channel composed of a series of elementary units (named bends) (Fig. 1b). The channel, horizontally placed, had a square cross section $A = l^2$ where $l = 2$ mm, and the elementary bend, which geometry was identical to the one used in Roudet et al. (2011), was characterized by a radius of curvature r_c of 1.5 mm and a straight length between two bends of 6.94 mm (see Fig. 1c). Every about 15 bends, there was a big bend, named "turning point", enabling to connect the two "straight" channel sections, which leads to change the flow direction in 180° and in order to have a long channel (the total developed straight length of the meandering channel $L = 1.37$ m), while keeping a compact device. The channel was curved in a PolyMethyl MethAcrylate (PMMA) plate (3 cm thick), and roofed over in a watertight manner by another plate (3 cm thick). The gas phase (air) was injected via a hole of diameter 1.6 mm, pierced perpendicularly to the channel; the gas injection was spaced from about eight bends from the liquid one so as to enable the liquid flow to be stable (Fig. 1b). Gas (air) was delivered from the supply pipeline regulated by a mass flow controller (Brooks® model 5850E). Before entering in the main channel, the gas flowed through a winding of a 2 m long capillary of 750 μm internal diameter, aiming at to increase the pressure drop in order to create a stable gas injection in the liquid flow. Liquid phase was pumped by a Cantoni® jet pump with the flow rate regulated by a mass flow control system (Micro motion®). The volumetric gas flow Q_G rates ranged from 0.2 to 9 L h^{-1} and liquid flow rates Q_L from 1 to 2 L h^{-1}. The corresponding superficial gas velocities j_G and liquid velocities j_L were: 0.014 m $s^{-1} \leq j_G = Q_G/l^2 \leq 0.625$ m s^{-1} and 0.069 m $s^{-1} \leq j_L = Q_L/l^2 \leq 0.139$ m s^{-1}.

2.4. Image acquisition system

The shadowgraph method was applied to investigate the gas-liquid hydrodynamics and mass transfer inside the meandering channel. The channel was lighted by a LitePad HO LED backlight (Rosco®) and the images of the bubbles flowing along the channel were recorded by a monochromatic high-speed CMOS camera (Photron® SA3) at 2000 frames per second. Image resolutions were 164 μm per pixel and 20 μm per pixel for the hydrodynamics and mass transfer experiments, respectively. The regions of interest were 168.1×84.2 mm^2 and 20.1×20.1 mm^2, respectively. For the mass transfer experiments, the gas-liquid flow was observed at 7 different axial distances X from the gas injection, namely: X = 0.02 m, 0.07 m, 0.12 m, 0.17 m, 0.22 m, 0.32 m and 0.42 m, as depicted in Fig. 1(b).

2.5. Image processing

2.5.1. Hydrodynamics of the gas-liquid flow

A typical raw image of the gas-liquid flow all along the channel length (1.37 m) is shown in Fig. 2(a). In order to extract the hydrodynamics parameters (gas hold-up, bubble length and

Table 1
Physio-chemical properties of the liquid phases at 293.15 K.

Liquid phase	C (g L^{-1})	σ_L (mN m^{-1})	μ_L (mPa s)	ρ_L (kg m^{-3})
Deionized water	0	71.4	1.003	996.8
Aqueous solution of glucose anhydrous and sodium hydroxide	20 20	76	1.118	1004.5
Aqueous solution of glucose anhydrous sodium hydroxide and resazurin	20 20 0.1	75	1.118	1004.5

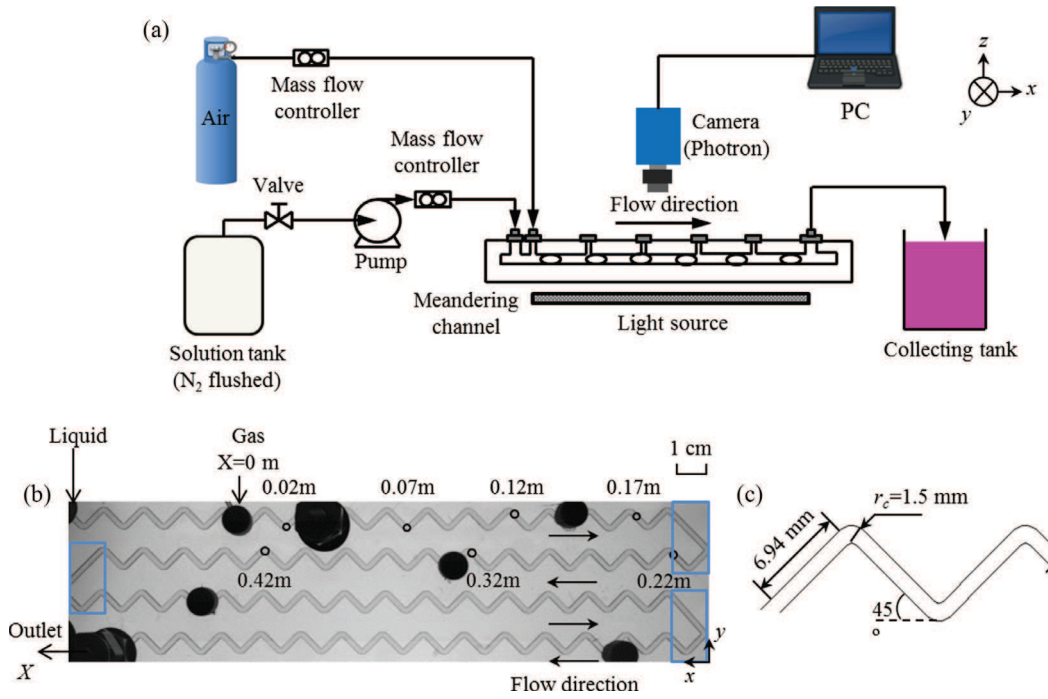

Fig. 1. (a) Schematic diagram of the experimental set-up. (b) Picture of the meandering channel in the horizontal *xy*-plan defined in (a). *X* corresponds to the location (curvilinear coordinate) in the channel from the gas inlet. $X = 0$ is the location where the two phases enter in contact. The channel has a cross-sectional area $A = 2 \times 2$ mm^2, and a total developed straight length L of 1.37 m. Black circles represent the axial positions where the equivalent oxygen concentration fields were measured. The sections of the channel corresponding to the so-called "turning points" are outlined by blue rectangles. The arrows indicate the flow direction. (c) Schematic of elementary units (bends) of the meandering channel.

velocity, liquid slug length etc.) from the raw image, a background image when the channel was filled with the liquid phase was needed, shown in Fig. 2(b). Then, an image post-treatment algorithm was implemented on the software Matlab (R2015a). In this algorithm, the background division approach was used to eliminate the effect of the background, instead of the traditional method consisting in subtracting to background image to each image; this was found to be more suitable to avoid illumination fluctuations and to diminish the confusion between background and foreground in pixels (Izquierdo-Guerra and García-Reyes, 2010). The image processing made possible the accurate detection of all the bubbles and liquid slugs inside the channel, as displayed in Fig. 2 (c) and (d) respectively, as below:

- For the gas bubbles image (Fig. 2c), it was generated by the segmentation methods in image processing and analysis in Matlab. Namely, after dividing the raw image (Fig. 2a) with the background image when the channel was filled with the liquid phase (Fig. 2b), one could obtain the image where only the bubbles left (not shown here). Then the image segmentation methods were implemented to identify all the bubbles on the image (Fig. 2c).
- For the liquid slugs image (Fig. 2d), it was generated by subtracting the image where only the channel left on the image with Fig. 2(c). The image where only the channel left on the image was obtained by dividing the background image when the channel was filled with the air phase (not shown here), with the one filled with the liquid phase (Fig. 2b).

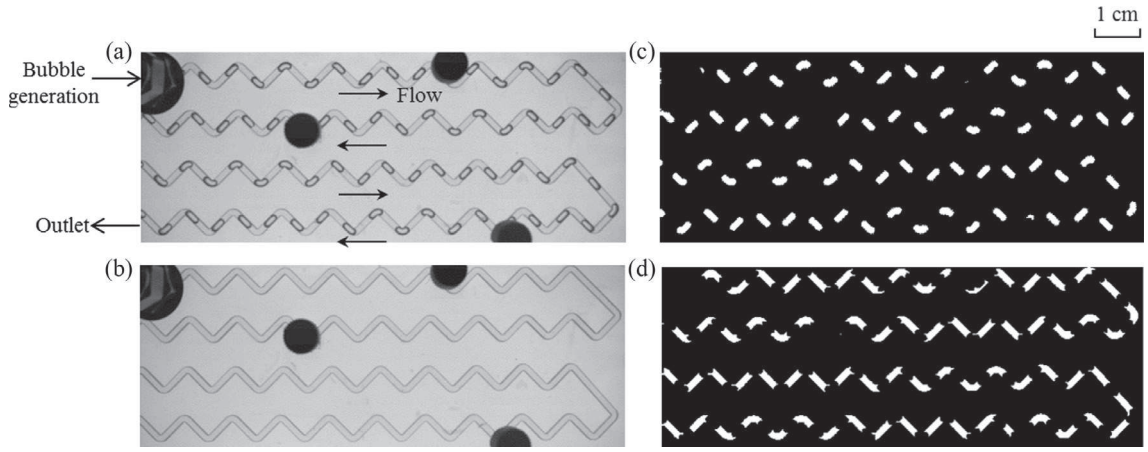

Fig. 2. Sequence of image processing. (a) Typical raw image of gas-liquid flows. (b) Raw image of the channel filled with liquid phase. (c) Detection of the bubbles (binary image). (d) Detection of the liquid slugs (binary image). Operating condition: $j_L = 0.139$ m s^{-1}, $j_G = 0.069$ m s^{-1}.

Once detected, the areas of the channel in the *xy*-plane (noted as A_C), all the 2D bubbles (A_B) and all the 2D liquid slugs (A_S) appearing along the whole length of the channel, could be obtained from the final binary images. Thus, the gas hold-up could be calculated as according to:

$$\varepsilon = \frac{A_B}{A_C} = \frac{A_B}{l \times L} = \frac{\sum A_{B,i}}{l \times L} \quad (1)$$

where $i = 1 \ldots N$, N is the number of bubbles/liquid slugs. It was observed that the difference between the summation of the bubble areas and liquid slug areas $(\sum A_{B,i} + \sum A_{s,i})$ and the channel area A_C is smaller than 2%, which could be attributed due to the area occupied by the liquid film.

Bubble characteristics (i.e. bubble length L_B, liquid slug length L_S, and bubble velocity U_B) were determined only in Taylor flow regime (defined in Section 3.1.1). The lengths of bubble and of liquid slug (noted L_B and L_S respectively, illustrated in Fig. 3a) were extracted from the major axis length of the bubbles which was an automatic procedure based on a pre-defined function. The averaged values of L_B and L_S were calculated by considering 20 bubbles on one image and 20 images were used. The bubble velocity U_B was deduced from the averaged times required by bubbles to flow along two bend periods. For a given operation condition, the standard deviations of the bubble characteristics (L_B, L_S and U_B) of all the bubbles inside the channel have found to be smaller than 6% of the averaged value.

2.5.2. Gas-liquid mass transfer

The gas-liquid mass transfer characteristics were determined by using the same image post-treatment algorithm (implemented on the software Matlab R2015a), than the one used by Dietrich et al. (2013). It consisted of two main steps: (i) the determination of the calibration curve, and (ii) the image processing which enabled to transform pixel-by-pixel the acquired grey-level images into the equivalent oxygen concentration fields. Note that the term "equivalent" was used because in reality the oxygen concentration in the liquid phase was null, oxygen being fully consumed by the instantaneous oxidation reaction.

For the calibration process, different concentrations of resazurin solution were prepared: 0, 0.025 g L^{-1}, 0.05 g L^{-1}, 0.075 g L^{-1} and 0.1 g L^{-1}. An example of calibration curve (at $X = 0.02$ m) is depicted in Fig. 3(b), showing the linearity between the grey levels and the equivalent amounts of oxygen transferred per unit of liquid volume. It is important to mention that the calibration process was re-implemented each time when the observation position (camera, light source, reactor) was changed. After applying the calibration curve in the image processing, the equivalent concentration field of oxygen could be obtained, and the oxygen transferred in the liquid slugs could be directly visualized, depicted in Fig. 3(c). Note that under the milli- scale conditions investigated, any oxygen concentration could be unfortunately measured in the liquid film zone close to the walls.

3. Results and discussion

3.1. Gas-liquid hydrodynamics

3.1.1. Flow regimes, overall gas hold-up and bubble velocity

Depending on the gas and liquid flow rates, different spatial distributions of the two phases were observed and various flow regimes were distinguished. The cartography of the gas-liquid flow regimes is displayed in Fig. 4. Under the present operating conditions ($0.014 \text{ m s}^{-1} \leq j_G \leq 0.625 \text{ m s}^{-1}$; $0.069 \text{ m s}^{-1} \leq j_L \leq 0.139 \text{ m s}^{-1}$), three regimes can be identified:

- The Taylor flow regime occurs at low and moderate gas flow rates, for which the lengths of bubbles and liquid slugs are constant along the meandering channel and regularly spaced. By visualization, one can observe that (i) the bubble length L_B increases as the gas flow rate increases under a given liquid flow rate; (ii) L_B decreases as the liquid flow rate increases under a given gas flow rate; (iii) the liquid slug length (separating two consecutive bubbles) significantly decreases as gas flow rate increases, whereas it slightly varies as liquid flow rate changes under a given gas flow rate.
- The second regime, called slug-annular flow regime, occurs at relatively high gas flow rates. Unstable slug flows appear, characterized by the occurrence of long bubbles. Two consecutive bubbles can be so close to each other that gas-liquid flow exhibits significant randomness. The rupture of an extremely long bubble could be seen under some conditions.
- The last regime is the annular flow and occurs at high gas flow rates. A continuous gas core in the channel center seems to be form.

The evolution of gas hold-up ε (measured over the whole length of the channel, see Eq. (1)) is plotted in Fig. 5 as a function of the volumetric quality (fraction) of gas $\beta = (Q_G/(Q_G + Q_L))$. A deviation

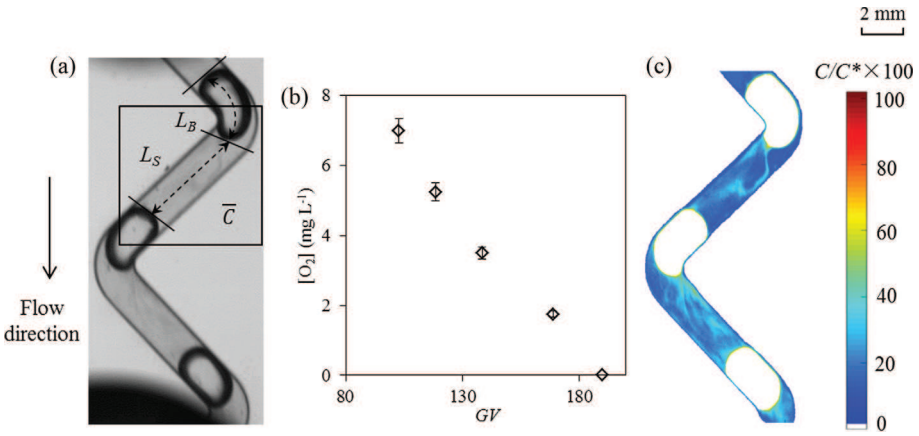

Fig. 3. Gas-liquid mass transfer experiments: (a) Typical raw image, where $\overline{C}$ corresponds to the averaged equivalent oxygen concentration in the liquid slug, and at this axial location in the meandering channel, $\overline{C}$ measured refers to the black rectangle. (b) Calibration curve between grey levels and equivalent amounts of oxygen transferred per unit of liquid volume. (c) Equivalent oxygen concentration field, $C(x, y)$, obtained after applying image processing and the calibration curve. Operating condition: $j_L = 0.139 \text{ m s}^{-1}$, $j_G = 0.069 \text{ m s}^{-1}$, flowing distance $X = 0.02$ m (close to the gas injection).

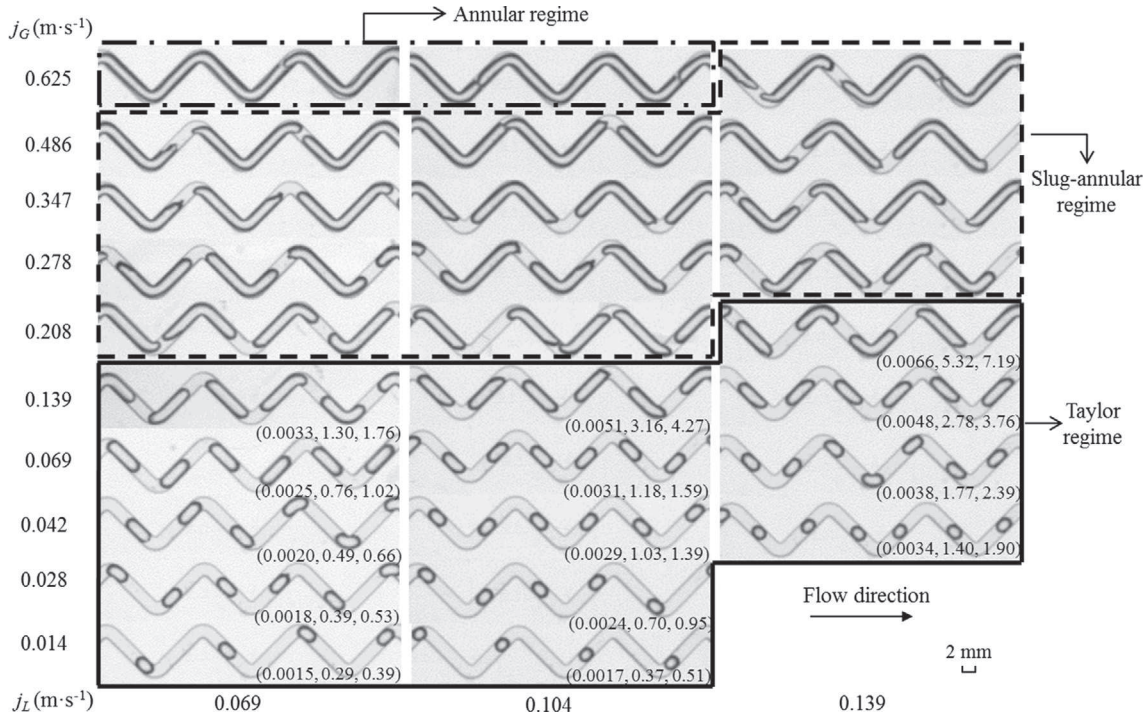

Fig. 4. Cartography of gas-liquid flow regimes. The flow regimes in the frame with solid lines correspond to the Taylor regime, with dashed lines the slug-annular regime, and with dash dotted lines the annular regime. The numbers in the brackets correspond to (*Ca, We, Ce*).

between ε and β could be observed leading to values of ε smaller thanβ. It can be explained by writing the mass balance of the gas phase, as:

$$A \cdot (j_G + j_L) \cdot \beta = A \cdot U_B \cdot \varepsilon \tag{2}$$

Due to the fact that the bubble travels slightly faster than predicted by the superficial two-phase velocity, ε should be logically smaller than β to verify this mass balance. The degree of deviation depends on the flow regime:

- relatively large for the Taylor flow (ranging from 1.17% to 15.95% with a mean deviation of 8.86%), confirming the occurrence of bubble slip velocity;
- moderate for the slug-annular flow, varying from 0.49% to 9.03% with a mean deviation of 4.46%;
- small for the annular flow, varying from 0.45% to 0.88% with a mean deviation of 0.67%.

Meanwhile, the Taylor flow regime is characterized by relatively low and moderate volumetric quality of gas β (between 0.17 and 0.67). Higher β lead to non-uniform bubble size distribution and irregular gas-liquid flow, like slug-annular flow, until reaching the annular flow regime for which β is up to 0.90.

The evolution of bubble velocity U_B as a function of the total superficial velocity j (equal to $j_G + j_L$) is plotted in Fig. 5(b). It can be observed that the values of U_B are always larger than those of

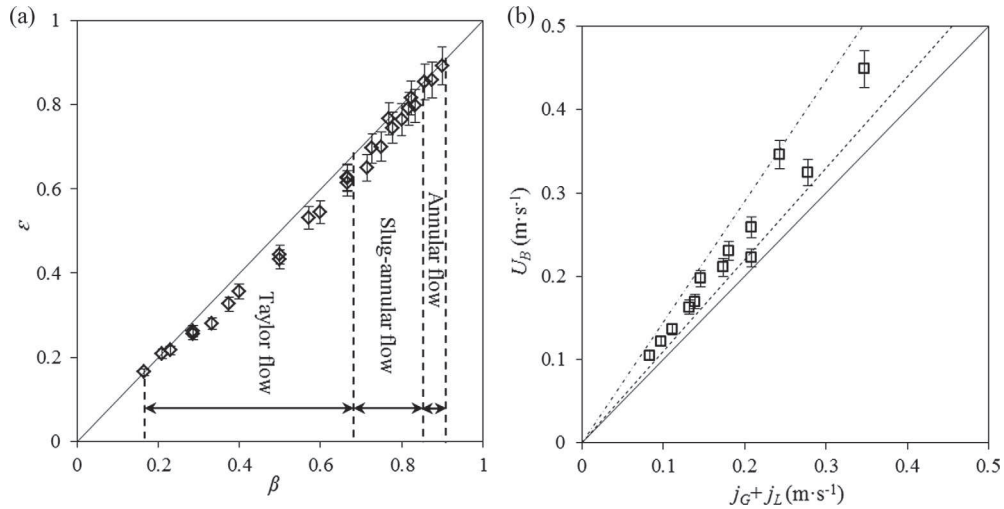

Fig. 5. (a) Evolution of gas hold-up as a function of the volumetric quality of gas in the meandering channel. The points inside the red dashed ellipse belong to Taylor flow. (b) Bubble velocity versus two-phase total superficial velocity. The solid line represents $U_B = j_G + j_L$, the dashed line $U_B = 1.1(j_G + j_L)$, the dash dotted line $U_B = 1.45(j_G + j_L)$.

j, thus indicating that there exists a slip phenomenon between bubbles and liquid film. The relationship between U_B and j could be usually correlated using the drift-model (Zuber and Findlay, 1965), as following:

$$U_B = C_0 \cdot j + U_d \tag{3}$$

where, in the case of vertical two-phase-flows, C_0 represents the distribution parameter, which takes into account the effect of non-uniform flow and concentration profiles, and U_d the drift velocity, which considers the effect of the local relative velocity. In our case, the distribution parameter C_0 equals to 1.27, which is consistent with the values encountered in the literature that vary between 0.85 and 1.38 (Tsoligkas et al., 2007); the drift velocity U_d equals to -0.0043 m s^{-1}.

3.1.2. Bubble length and slug length

For the operating conditions corresponding to the Taylor regime ($0.014 \text{ m s}^{-1} \leq j_G \leq 0.208 \text{ m s}^{-1}$ and $0.069 \text{ m s}^{-1} \leq j_L \leq 0.13\,9 \text{ m s}^{-1}$), the dimensionless Bond number $Bo = \rho_L \cdot g \cdot l^2/\sigma$ equals to 0.52, the Weber numbers $We = \rho_L \cdot U_B^2 \cdot l/\sigma_L$ range from 0.29 to 5.32, the capillary numbers $Ca = \mu_L \cdot U_B/\sigma_L$ from 0.0015 to 0.0066 and the Reynolds numbers $Re = \rho_L \cdot U_B \cdot l/\mu_L$ from 188 to 806. For meandering channels, one should also consider the dimensionless number comparing the centrifugal forces and capillary effects, defined as $Ce = \rho_L \cdot U_B^2 \cdot l^2/\sigma_L \cdot r_c$: it ranges from 0.39 to 7.19.

The relationship between the normalized bubble length L_B/l and the ratio of gas superficial velocity and liquid superficial velocity, $\alpha = j_G/j_L$, is plotted in Fig. 6(a). Typically, the smallest and largest bubble lengths are 2.53 mm and 8.22 mm respectively, corresponding to the normalized bubble length by the width of channel L_B/l from 1.27 to 4.11. It is important to precise that no obvious decrease of L_B was observed along the axial distance X (not shown here), indicating that the compressibility effects of the gas phase are negligible in the channel. Garstecki et al. (2006) observed that for T-junctions with aspect ratio greater than or equal to 1, the squeezing mechanism was expected to dominate the bubble formation for $Ca < 0.01$. Therefore, a simple scaling law was proposed to predict the bubble length, as below:

$$\frac{L_B}{l} = 1 + \lambda \cdot \frac{j_G}{j_L} \tag{4}$$

where the value of λ depends on the geometry of the T-junction. It can be seen from Fig. 6(a) that the linear evolution between L_B/l and j_G/j_L is experimentally verified, which would indicate that the squeezing mechanism is suitable to predict the bubble length. In the present study, by using the linear least square regression method, it can be obtained:

$$\frac{L_B}{l} = 1 + 1.69 \cdot \frac{j_G}{j_L}, \text{ mean deviation : } 6.40\% \tag{5}$$

The present value of λ is larger in comparison with the one obtained by Roudet et al. (2011) (equals 1.13). This could be explained by the fact that in Roudet et al. (2011), the experiments were not carried out in aqueous solutions of glucose and sodium hydroxide, but in water, and also that the channel's wettability could have changed.

Fig. 6(b) plots the variation of normalized slug length L_S/l as a function of j_G/j_L. It can be observed that for a given j_L, L_S/l first decreases significantly with the increase of j_G/j_L, and then changes slightly, but remain slightly dependent on j_L. This is consistent with the literature (Qian and Lawal, 2006; Leclerc et al., 2010; Roudet et al., 2011; Abadie et al., 2012). Regression of the experimental data provides the following correlation:

$$L_S/l = 1.87 \cdot \left(\frac{j_G}{j_L}\right)^{-0.5}, \text{ mean deviation : } 8.6\% \tag{6}$$

The value of the power of j_G/j_L underlines the predominant contribution of the flow rate ratio to L_S.

Table 2 summarizes all the measured bubble characteristics.

3.1.3. Bubble shape

In the Taylor flow regime, the cartography of bubble shape displayed in Fig. 4 shows that depending on the dimensionless numbers (Ca,We,Ce), the bubble shape changes. It can be observed that:

when $Ca < 0.003$, the bubble shape is slightly deformed, which is in agreement with what was observed in the creeping flow ($Ca < 0.01$) by Giavedoni and Saita (1999). However, in the present study ($0.0015 < Ca < 0.0066$), not only the viscous force could be attributed to the bubble shape, but also the inertial force ($0.29 < We < 5.32$).

When $We < 1.40$, the nose and rear menisci of the bubble could be well described as two hemispherical caps; however, when $We > 1.40$, the front meniscus goes flat, while the rear meniscus turns slender. This phenomena is consistent with the one observed by Roudet et al. (2011), which the bubble changes in shape were observed when $We > 1.5$.

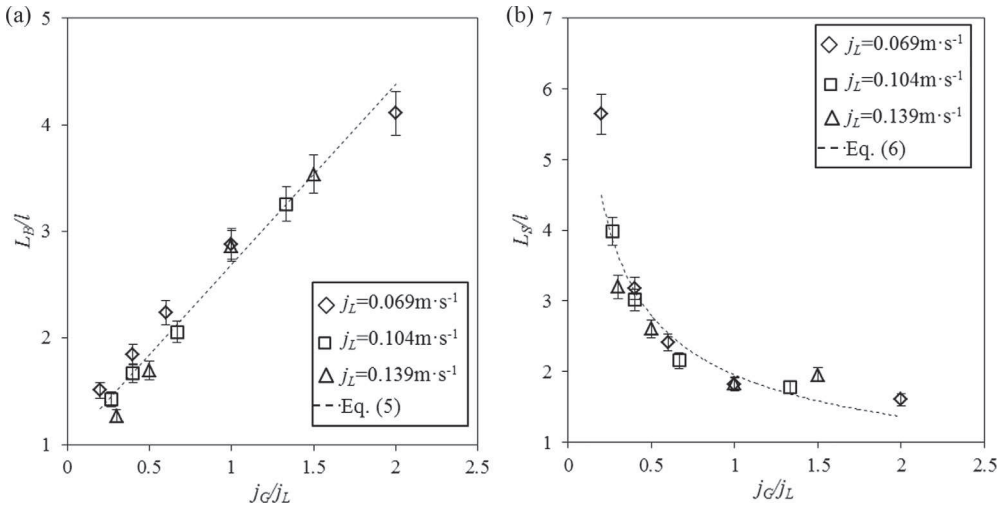

Fig. 6. (a) Normalized bubble length and (b) normalized slug length versus gas liquid flow rate ratio for varying liquid phase velocities in Taylor flow regime in the meandering channel.

Table 2
Bubble characteristics versus gas and liquid flow rates in the meandering channel. k_La_{Roudet} represent the values obtained by Roudet et al. (2011) under the same operating conditions in meandering channel.

j_L (m s^{-1})	j_G (m s^{-1})	U_B (m s^{-1})	Re	L_B (mm)	L_S (mm)	e	a (m^{-1})	k_La (s^{-1})	k_La_{Roudet} (s^{-1})	k_L (m s^{-1})
0.069	0.014	0.105	188.6	3.02	11.29	0.786	442	0.115		2.60×10^{-4}
0.069	0.028	0.122	218.5	3.69	6.35	0.883	727	0.128		1.76×10^{-4}
0.069	0.042	0.136	245.3	4.48	4.82	0.925	932	0.147		1.58×10^{-4}
0.069	0.069	0.169	304.5	5.76	3.63	0.959	1216	0.157	0.148	1.29×10^{-4}
0.069	0.139	0.222	399.0	8.22	2.90	0.978	1600	0.207	0.279	1.29×10^{-4}
0.104	0.028	0.163	292.7	2.85	7.97	0.805	554	0.232		4.19×10^{-4}
0.104	0.042	0.197	354.2	3.34	6.03	0.886	725	0.254		3.51×10^{-4}
0.104	0.069	0.211	379.0	4.12	4.31	0.914	1001	0.269		2.69×10^{-4}
0.104	0.139	0.346	621.4	6.51	3.57	0.966	1384	0.353		2.55×10^{-4}
0.139	0.042	0.230	414.3	2.53	6.40	0.808	607	0.309		5.09×10^{-4}
0.139	0.069	0.259	465.1	3.39	4.21	0.886	846	0.324	0.239	3.83×10^{-4}
0.139	0.139	0.324	583.1	5.73	3.67	0.947	1226	0.387	0.441	3.16×10^{-4}
0.139	0.208	0.449	806.5	7.07	3.91	0.976	1442	0.446		3.09×10^{-4}

When the bubble passes the bends, the centrifugal effect becomes essential. Compared with the inertial forces, the centrifugal forces have the same order of magnitude ($0.39 < Ce < 7.19$), thus the bubble shape is distorted by the contributions from both two forces. When $Ce < 1.90$, the extent of distortion of the bubble is slight; by increasing Ca, We and Ce, the bubble deformation appear to be more pronounced.

3.1.4. Interfacial area

The Taylor bubbles flowing in the meandering channel were not only affected by inertial effects, but also by the centrifugal effects induced by their passage in the periodic bends (see Figs. 3 and 4). These shape distortions imply that the bubbles cannot be described, as classically done, by two hemispherical caps for the bubble nose and rear, with a cylindrical shape for the bubble body. As a consequence, the bubbles were considered as prolate ellipsoid, leading to

$$S_B = \frac{\pi \times l^2}{2} \times \left[1 + \frac{L_B}{l \cdot e} \arcsin(e)\right] \tag{7}$$

$$V_B = \frac{\pi \times l^2 \times L_B}{6} \tag{8}$$

where S_B and V_B represent the surface and the volume of the bubble, respectively, and e is the eccentricity of the ellipsoidal bubble, $e^2 = 1 - \frac{l^2}{L_B^2}$. For the conventional gas-liquid contactors, the definition of interfacial area a can be as follow:

$$a = \frac{S_G}{V_T} \tag{9}$$

where S_G is the total surface of the bubbles in the contactor, and V_T the whole volume of gas and liquid phases. In our case, due to the fact that one unit cell, which is constituted of one bubble and one liquid slug, appears repeatedly along the channel for Taylor flow regime, it can define a as below:

$$a = \frac{S_B}{V_{UC}} = \frac{S_B}{V_L + V_B} \tag{10}$$

where V_{UC} is the volume of one unit cell, and V_L the volume of the liquid phase, which includes the volume of liquid slug and liquid film. As the gas fraction $\beta = Q_G/(Q_G + Q_L) = V_B/(V_B + V_L)$, Eq. (10) can be rewritten as:

$$a = \beta \times \frac{S_B}{V_B} = \beta \times \frac{3}{L_B} \times \left[1 + \frac{L_B}{l \cdot e} \arcsin(e)\right] \tag{11}$$

Fig. 7 plots the evolution of a as a function of β. It shows that a perfect linear relationship exists between a and β. From Eq. (11), it can be known that the slope represents the ratio of S_B and V_B, namely, no matter how L_B varies, $\frac{S_B}{V_B}$ remains almost constant. The values of a, ranged from 400 to 1600 m^{-1}, are reported in Table 2 for the different operating conditions.

3.2. Gas-liquid mass transfer

With the colorimetric technique, it is possible to locally visualize the oxygen transferred in the liquid slugs as far as the bubbles moves along the channel length. Both the evolution of equivalent O_2 concentration fields in the liquid slug and the quantitative characterization of the O_2 transferred could be obtained from the image processing, which will be described in the following subsections, respectively.

3.2.1. Equivalent O_2 concentration fields

Firstly, for illustrative purpose, Fig. 8a presents the temporal evolution of the equivalent O_2 concentration fields in a liquid slug located before a bubble, from the moment right after the bubble pinch-off to the following times when the bubble flows along the bends ($j_L = 0.139$ m s^{-1}, $j_G = 0.069$ m s^{-1}). It can be observed that at the beginning ($t = 0$ ms, bubble right after the pinch-off):

- Oxygen accumulates in the front of the bubble: this is a consequence of the bubble formation stage, during which the transfer of oxygen mainly occurs in the front part of the bubble. This is consistent with what has been observed in the straight channel (see Yang et al., 2016b).

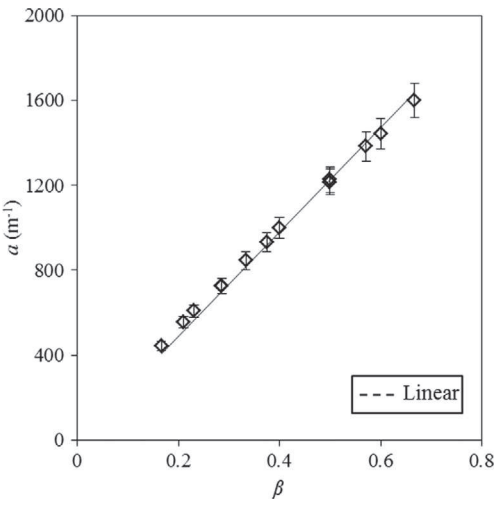

Fig. 7. Evolution of the interfacial area a as a function of gas fraction β.

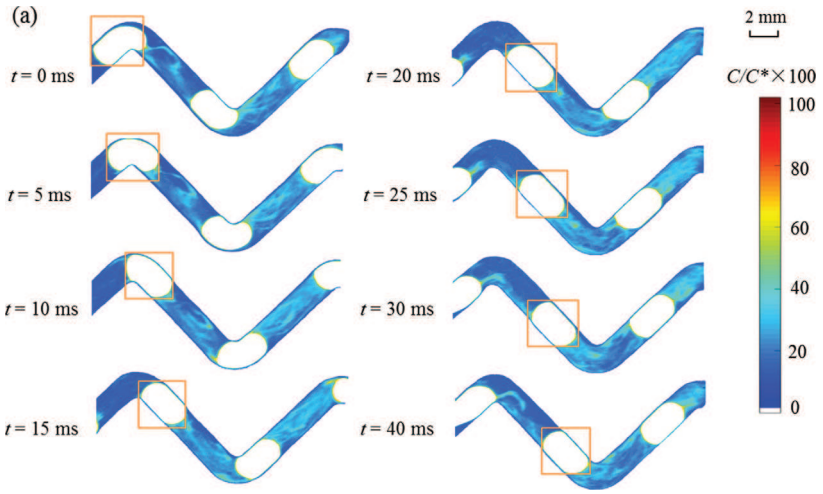

Fig. 8a. Temporal evolution of the equivalent oxygen concentration fields in a liquid slug, from the moment right after the bubble pinch-off to the following times where the observed bubble moves in the meandering channel (operating condition: $j_L = 0.139$ m s^{-1}, $j_G = 0.069$ m s^{-1}, flow direction from left to right). The bubble in the orange rectangle represents the bubble observed.

– Several filaments of higher O_2 concentration can be distinguished in the liquid slug. Two non-symmetrical recirculation zones with respect to the channel centerline could be identified, whereas in straight channels, two recirculation loops symmetrical and equal in size take place.

When the liquid slug moves in the straight section between two bends ($t = 5$ ms and $t = 10$ ms), the amount of oxygen accumulated just in the front of the bubble tends to decrease as progressively transported towards the liquid slug core; the recirculation zones are also growing, until reaching to the first bend ($t = 15$ ms). At this location, they are twisted and split up. Then, the passage through a bend affects significantly the shape and locations of these recirculation zones, and more generally the structure of the flow in the liquid slug. These distortions of the filaments of higher oxygen concentrations can be explained by the centrifugal effects induced by the channel curvature and the occurrence of the Dean vortices (Anxionnaz-Minvielle et al., 2013; Dai et al., 2015b). Herein, the mixing in the liquid slugs can be enhanced, the change in equivalent oxygen concentration fields in the liquid slugs as far as the bubbles moves is an indirect measure of this phenomenon ($t = 20$–40 ms).

The corresponding temporal evolution of the amount of transferred O_2 in the liquid slug is displayed in Fig. 8b. A kind of critical point seems to exist corresponding to the time where the recirculation zones are passing the bend ($t = 20$ ms). Before this point, the slope of the curve is higher than the one after the point. This would highlight first the contribution of the bubble formation stage to the mass transfer, and then a slowed-down mass transfer due to the mixing effect induced by the bend that could decreases the average driving force in the liquid slugs. Deeper investigations would be required to confirm this first trend.

Fig. 9 shows the evolution of O_2 concentration fields in the liquid slug obtained at different axial positions ($X = 0.02$, 0.07, 0.12, 0.17, 0.22, 0.32 and 0.42 m) along the meandering channel ($j_L = 0.139$ m s^{-1}, $j_G = 0.069$ m s^{-1}). It can be seen that the equivalent O_2 concentration level in the liquid slugs is getting greater and greater, until reaching an almost saturated state at $X = 0.42$ m. The apparent recirculation zones inside the liquid slugs also tend to disappear as far as flowing in the channel and thus the concentration fields become more and more uniform in the liquid slugs. This indicates that after several bends (about 20 bends), the gradient of O_2 concentration within the liquid slug no longer exists.

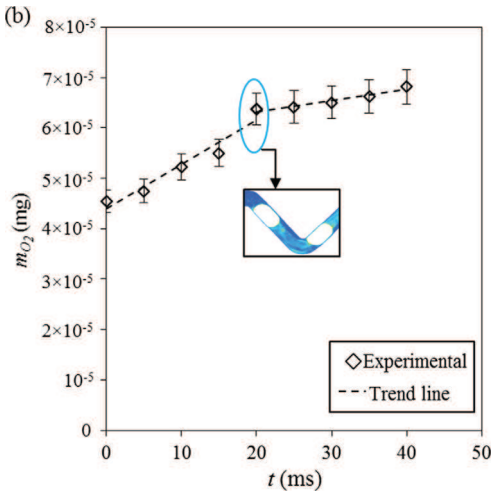

Fig. 8b. Evolution of the amount of transferred oxygen in the liquid slug as a function of time, from the moment right after the bubble pinch-off to the following times where the observed bubble moves in the meandering channel (operating condition: $j_L = 0.139$ m s^{-1}, $j_G = 0.069$ m s^{-1}).

The accumulation of O_2 at the front and at the rear of the bubble can be observed along the first bends, and tend to disappear, as the recirculation zones, for the higher axial locations, namely when the liquid slugs become almost perfectly mixed.

For different hydrodynamic conditions, a comparison of the equivalent O_2 concentration fields, observed at the axial position $X = 0.07$ m is proposed in Fig. 10. It can be logically observed that increasing the gas flow rate (and thus the bubble length) under a given liquid flow rate (i.e. Fig. 10a and b, or Fig. 10c and d, or e and f) leads to a rise in the amount of oxygen transferred in the liquid slugs. The opposite effect is observed for increasing the liquid flow rate (and thus the liquid slug length) at a given gas flow rate.

3.2.2. Overall gas-liquid mass transfer coefficient

The equivalent O_2 concentration at the point (x, y) in the liquid slug could be extracted from the image processing, noted as $C(x, y)$. It is important to remind that the equivalent O_2 concentration field obtained at a given location (x, y) is a mean value along the z-axis

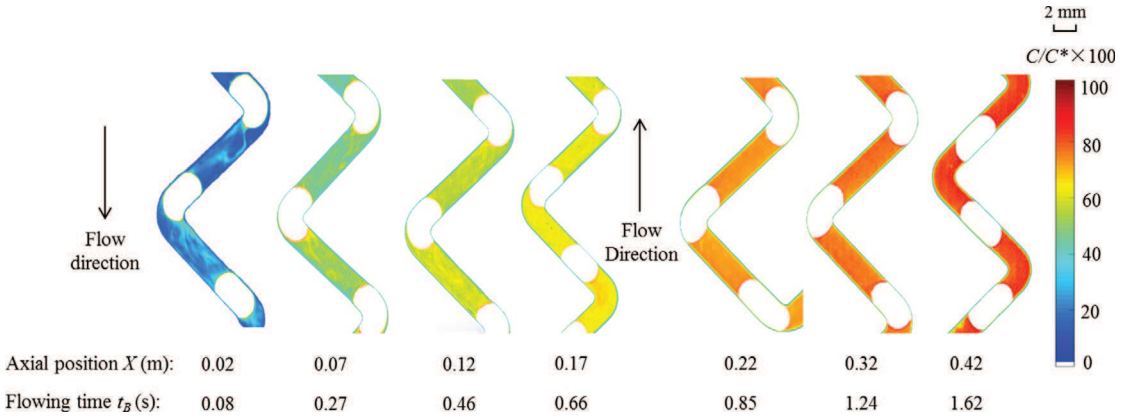

Fig. 9. Evolution of the equivalent oxygen concentration fields in the liquid slug as a function of the axial position in the meandering channel. Operating condition: $j_L = 0.139$ m s^{-1}, $j_G = 0.069$ m s^{-1}.

(Dietrich et al., 2013), no discrimination of the equivalent oxygen concentration fields related to each *xy*-plane being possible along the channel height. Therefore the mass flux of O_2 transferred per unit of bubble surface at a given axial position X, noted as $\varphi_{O_2}(X)$, can be calculated as below:

$$\varphi_{O_2}(X) = \frac{\iiint C(x,y) \times dx \times dy \times dz}{S_B \times t_B} \tag{12}$$

where t_B is the time for a bubble for flowing to the axial position X after the pinch-off, which is defined according to X/U_B, S_B the bubble surface, which can be calculated from Eq. (7).

Fig. 11 (a) illustrates the evolution of φ_{O_2} in the liquid slug as a function of X under various j_L at a given $j_G = 0.042\text{m} \cdot \text{s}^{-1}$. It clearly appears that φ_{O_2} is not constant at all along the channel length: higher values are observed for the axial positions close to the gas injection ($X < 0.02$ m). Such result is consistent with the observations made in our previous work (Yang et al., 2016b), where it was outlined how the bubble formation stage could accelerate the mass transfer, when compared to the flowing stage. Then, the value of φ_{O_2} decreases significantly as the bubble moves along the meandering channel, and tends to reach a plateau after $X = 0.3$ m.

The averaged equivalent O_2 concentration, $\overline{C}$, in the liquid slug of the unit cell (see Fig. 3a) can be also calculated, at the given axial position X, from the integration of the equivalent oxygen concentration field in a unit cell, or more precisely in the liquid slug as no information could be acquired in the liquid film close to the walls. This can be expressed as below:

$$\overline{C} = \frac{\iiint C(x,y) \times dx \times dy \times dz}{L_{UC} \times l^2} \tag{13}$$

Note that as the visualization of the bubble areas of the nose and rear is also not available due to their ellipsoidal shape, the liquid volume linked to these bubble areas cannot be taken into

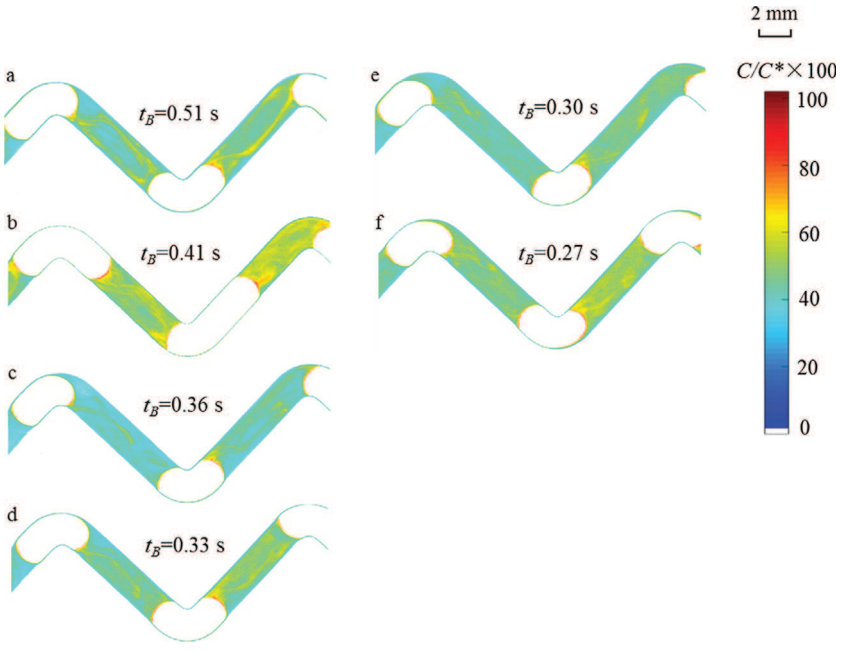

Fig. 10. Comparison of the equivalent oxygen concentration fields in the liquid slug under various operating conditions: (a) $j_L = 0.069$ m s^{-1}, $j_G = 0.042$ m s^{-1}; (b) $j_L = 0.069$ m s^{-1}, $j_G = 0.069$ m s^{-1}; (c) $j_L = 0.104$ m s^{-1}, $j_G = 0.042$ m s^{-1}; (d) $j_L = 0.104$ m s^{-1}, $j_G = 0.069$ m s^{-1}; (e) $j_L = 0.139$ m s^{-1}, $j_G = 0.042$ m s^{-1}; (f) $j_L = 0.139$ m s^{-1}, $j_G = 0.069$ m s^{-1}. Axial position X equals to 0.07 m.

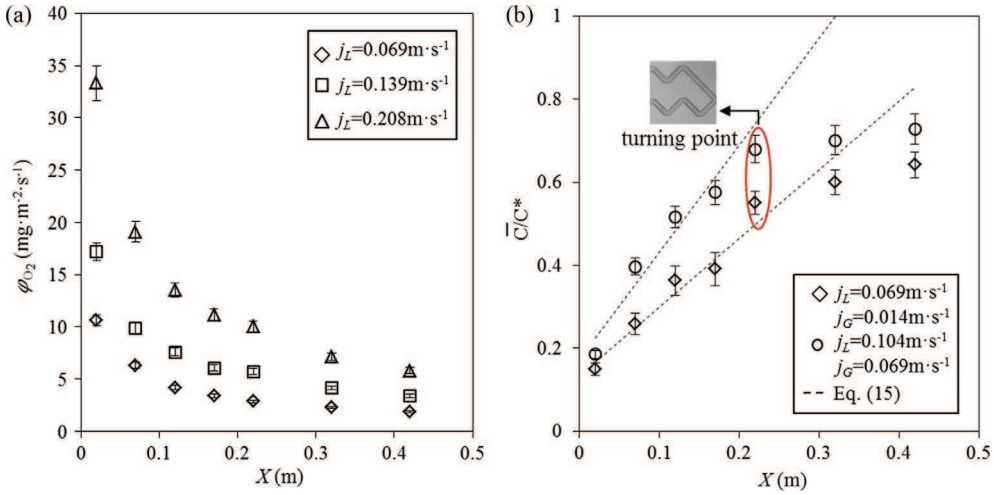

Fig. 11. (a) Evolution of mass flux of the transferred oxygen φ_{O_2} per unit of bubble surface as a function of the axial position X under various liquid superficial velocities j_L at a given gas superficial velocity j_G = 0.042 m·s^{-1}. (b) Comparison of the evolution of normalized average oxygen concentration in the liquid slug along the channel with the ones predicted by the plug flow model. For j_L = 0.069 m s^{-1}, j_G = 0.014 m s^{-1}, Re = 188; j_L = 0.104 m s^{-1}, j_G = 0.069 m s^{-1}, Re = 379.

account for the calculation. It has been estimated that this bias could lead to a maximum error of 13% on the volume estimation of liquid phase in a unit cell.

Fig. 11(b) shows the evolution of the normalized averaged O_2 concentration $\overline{C}/C^*$ (C^* being the O_2 concentration at saturation) in the liquid slug as a function of the axial position X in the channel, under various gas superficial velocities j_G and at given liquid superficial velocity j_L = 0.069 m s^{-1}. It can be observed that $\overline{C}/C^*$ increases as the gas superficial velocity increases under the given liquid superficial velocity, which is consistent with the visualization presented in Fig. 10.

For Taylor flow, the liquid phase consists in a series of mixed slugs, and then the plug-flow model is often used for mass transfer purposes. Uniform velocity and concentration over the channel cross section are then assumed, without taking into account the real structure of the flow in the liquid slug, for example, recirculation loops (Berčič and Pintar, 1997; Shao et al., 2010). Based on an oxygen mass balance on the liquid slug, it can be written (Roudet et al., 2011):

$$\varphi_{O_2}(X) = j_L \cdot \frac{d\overline{C}}{dX} = k_L \cdot a \cdot [C^* - \overline{C}(X)] \tag{14}$$

In the present case, the concentration of oxygen, $\overline{C}(X)$ is null as fully consumed by the reaction in reality, leading to

$$\frac{\overline{C}}{C^*} = \frac{k_L a \times X}{j_L} \tag{15}$$

where $k_L a$ represents the volumetric mass transfer coefficient, s^{-1}.

There exists then a linear relationship between $\overline{C}/C^*$ and X, and the slope stands for $k_L a/j_L$. Once applied, it has been found that Eq. (15) could predict well the experimental values of $\overline{C}/C^*$ only for Re < 300; for Re > 300, the deviation becomes higher than 18%. Typical examples of the comparison between the experimental and predicted evolutions of $\overline{C}/C^*$ are displayed in Fig. 11(b). Note that, when a fitting of the experimental values of $\overline{C}/C^*$ with X is applied (taking X = 0.02 m as a reference), different values are obtained at X = 0; this could be explained by the contribution of the bubble formation stage to the overall mass transfer. Fig. 11(b) also reveals that, for Re > 300, the prediction of Eq. (15) are relevant only before the axial positions below X = 0.22 m. As shown in Fig. 1(b), this specific location corresponds to the big bend (called "turning point"), namely to the location where the flow direction is changed in 180°. After X = 0.22 m, $\overline{C}/C^*$ is underestimated by the model, indicating that the big bend leads to slow down the flux of oxygen transferred (this is observed for all the operating conditions when Re > 300). More in-depth investigation of the velocity field structure of the two-phase flow when crossing the turning point would be required to explain this phenomenon.

The overall volumetric mass transfer coefficients deduced from the fitting between Eq. (15) with the experimental points just before the turning point, $k_L a$, are reported in Table 2. They are ranged from 0.1 to 1 s^{-1}, which the order of magnitude is in agreement with the values reported by Roudet et al. (2011). This can verify the feasibility of the colorimetric technique. As already observed in the literature (Nieves-Remacha et al., 2013; Yao et al., 2014), $k_L a$ increases when the gas superficial velocity j_G increases and when the liquid superficial velocity j_L increases. It is important to keep in mind that these overall volumetric mass transfer coefficients are just global parameters representing the inverse of characteristic time of mass transfer. The values here estimated remind approximate due to the assumptions made in the modelling (plug-flow) and to the fact that the contribution of the film in not taken into account.

At last, as the interfacial area a can be calculated by the assumption of the bubbles as prolate ellipsoid (see Section 3.1.4), the liquid-side mass transfer coefficient before the turning point k_L can be calculated by dividing $k_L a$ with a. As shown in Table 2, for a givenj_G, k_L increases with increasingj_L, and is less sensitive to the gas superficial velocity.

4. Conclusion

The colorimetric technique proposed by Dietrich et al. (2013), which was based on an oxygen-sensitive dye, was implemented to locally visualize and characterize the gas-liquid mass transfer in a square meandering millimetric channel. The hydrodynamics characteristics was first investigated in the channel, in terms of gas-liquid flow regime, gas hold-up, bubble length and velocity, liquid slug length and interfacial area. The oxygen concentration field inside the liquid slugs was then visualized at different axial positions. The non-symmetrical recirculation zones inside the liquid slug were observed to be twisted and split by the periodic bends, and tended to disappear as the bubble moving within the channel; the O_2 concentration inside the liquid slug became uni-

form after passing through several bends (around 20 bends). The occurrence of the "turning point" (i.e. the big bend enabling the flow direction in 180°) seemed to induce a slowing down of the mass transfer, especially when $Re > 300$ and $Ca > 0.002$. The mass flux of O_2 transferred per unit of bubble surface was significantly higher close to the gas injection due to the bubble formation stage, then it decreases significantly as the bubble flowing along the meandering channel, and becomes small after $X = 0.3$ m due to the decreasing driving force for the mass transfer. At last, by coupling this local information with a plug-flow model, overall volumetric mass transfer coefficients could be estimated. All these findings give important information to understand the gas-liquid mass transfer complex mechanism occurring in the meandering channel, which would serve as basis for implementing gas-liquid reaction in HEX reactors.

Acknowledgments

The financial assistance provided by the China Scholarship Council for L. Yang is gratefully acknowledged.

References

Abadie, T., Aubin, J., Legendre, D., Xuereb, C., 2012. Hydrodynamics of gas–liquid Taylor flow in rectangular microchannels. Microfluid. Nanofluid. 12, 355–369. http://dx.doi.org/10.1007/s10404-011-0880-8.

Anxionnaz, Z., 2009. Etude de l'influence de la géométrie des canaux sur les performances d'un réacteur/échangeur. University of Toulouse.

Anxionnaz, Z., Cabassud, M., Gourdon, C., Tochon, P., 2008. Heat exchanger/reactors (HEX reactors): concepts, technologies: State-of-the-art. Chem. Eng. Process. Process Intensif. 47, 2029–2050. http://dx.doi.org/10.1016/j.cep.2008.06.012.

Anxionnaz-Minvielle, Z., Cabassud, M., Gourdon, C., Tochon, P., 2013. Influence of the meandering channel geometry on the thermo-hydraulic performances of an intensified heat exchanger/reactor. Chem. Eng. Process. Process Intensif. 73, 67–80. http://dx.doi.org/10.1016/j.cep.2013.06.012.

Berčič, G., Pintar, A., 1997. The role of gas bubbles and liquid slug lengths on mass transport in the Taylor flow through capillaries. Chem. Eng. Sci. 52, 3709–3719. http://dx.doi.org/10.1016/S0009-2509(97)00217-0.

Butler, C., Cid, E., Billet, A.-M., 2016. Modelling of mass transfer in Taylor flow: investigation with the PLIF-I technique. Chem. Eng. Res. Des. 0–18. http://dx.doi.org/10.1016/j.cherd.2016.09.001.

Commenge, J.-M., Falk, L., 2014. Methodological framework for choice of intensified equipment and development of innovative technologies. Chem. Eng. Process. Process Intensif. 84, 109–127. http://dx.doi.org/10.1016/j.cep.2014.03.001.

Dai, Z., Fletcher, D.F., Haynes, B.S., 2015a. Influence of tortuous geometry on the hydrodynamic characteristics of laminar flow in microchannels. Chem. Eng. Technol. 38, 1406–1415. http://dx.doi.org/10.1002/ceat.201400752.

Dai, Z., Fletcher, D.F., Haynes, B.S., 2015b. Impact of tortuous geometry on laminar flow heat transfer in microchannels. Int. J. Heat Mass Transf. 83, 382–398. http://dx.doi.org/10.1016/j.ijheatmasstransfer.2014.12.019.

Darvas, F., Dorman, G., Hessel, V., 2014. Flow Chemistry. De Gruyter Textbook, Berlin, Boston.

Dessimoz, A.-L., Raspail, P., Berguerand, C., Kiwi-Minsker, L., 2010. Quantitative criteria to define flow patterns in micro-capillaries. Chem. Eng. J. 160, 882–890. http://dx.doi.org/10.1016/j.cej.2010.01.011.

Dietrich, N., Loubière, K., Jimenez, M., Hébrard, G., Gourdon, C., 2013. A new direct technique for visualizing and measuring gas–liquid mass transfer around bubbles moving in a straight millimetric square channel. Chem. Eng. Sci. 100, 172–182. http://dx.doi.org/10.1016/j.ces.2013.03.041.

Elgue, S., Aillet, T., Loubiere, K., Conté, A., Dechy-Cabaret, O., Prat, L., Horn, C.R., Lobet, O., Vallon, S., 2015. Flow photochemistry: a meso-scale reactor for industrial applications. Chim. Oggi/Chem. Today 33, 58–61.

Fries, D.M., von Rohr, P.R., 2009. Liquid mixing in gas–liquid two-phase flow by meandering microchannels. Chem. Eng. Sci. 64, 1326–1335. http://dx.doi.org/10.1016/j.ces.2008.11.019.

Garstecki, P., Fuerstman, M.J., Stone, H.a., Whitesides, G.M., 2006. Formation of droplets and bubbles in a microfluidic T-junction—scaling and mechanism of break-up. Lab Chip 6, 437. http://dx.doi.org/10.1039/b510841a.

Giavedoni, M.D., Saita, F.A., 1999. The rear meniscus of a long bubble steadily displacing a Newtonian liquid in a capillary tube. Phys. Fluids 11, 786. http://dx.doi.org/10.1063/1.869951.

Gourdon, C., Elgue, S., Prat, L., 2015. What are the needs for Process Intensification? Oil Gas Sci. Technol. – Rev. d'IFP Energies Nouv. 70, 463–473. http://dx.doi.org/10.2516/ogst/2014051.

Günther, A., Khan, S.a., Thalmann, M., Trachsel, F., Jensen, K.F., 2004. Transport and reaction in microscale segmented gas–liquid flow. Lab Chip 4, 278–286. http://dx.doi.org/10.1039/B403982C.

Haase, S., Murzin, D.Y., Salmi, T., 2016. Review on hydrodynamics and mass transfer in minichannel wall reactors with gas–liquid Taylor flow. Chem. Eng. Res. Des. 113, 304–329. http://dx.doi.org/10.1016/j.cherd.2016.06.017.

Haghnegahdar, M., Boden, S., Hampel, U., 2016. Mass transfer measurement in a square milli-channel and comparison with results from a circular channel. Int. J. Heat Mass Transf. 101, 251–260. http://dx.doi.org/10.1016/j.ijheatmasstransfer.2016.05.014.

Izquierdo-Guerra, W., García-Reyes, E., 2010. Background division, a suitable technique for moving object detection. In: Iberoamerican Congress on Pattern Recognition. Springer, Berlin, Heidelberg, pp. 121–127. http://dx.doi.org/10.1007/978-3-642-16687-7_20.

Karale, C.M., Bhagwat, S.S., Ranade, V.V., 2013. Flow and heat transfer in serpentine channels. AIChE J. 59, 1814–1827. http://dx.doi.org/10.1002/aic.13954.

Kherbeche, A., Milnes, J., Jimenez, M., Dietrich, N., Hébrard, G., Lekhlif, B., 2013. Multi-scale analysis of the influence of physicochemical parameters on the hydrodynamic and gas–liquid mass transfer in gas/liquid/solid reactors. Chem. Eng. Sci. 100, 515–528. http://dx.doi.org/10.1016/j.ces.2013.06.025.

Kuhn, S., Jensen, K.F., 2012. A pH-sensitive laser-induced fluorescence technique to monitor mass transfer in multiphase flows in microfluidic devices. Ind. Eng. Chem. Res. 51, 8999–9006. http://dx.doi.org/10.1021/ie300978n.

Leclerc, A., Philippe, R., Houzelot, V., Schweich, D., de Bellefon, C., 2010. Gas-liquid Taylor flow in square micro-channels: new inlet geometries and interfacial area tuning. Chem. Eng. J. 165, 290–300. http://dx.doi.org/10.1016/j.cej.2010.08.021.

Nieves-Remacha, M.J., Kulkarni, A.A., Jensen, K.F., 2013. Gas-liquid flow and mass transfer in an advanced-flow reactor. Ind. Eng. Chem. Res. 52, 8996–9010. http://dx.doi.org/10.1021/ie4011707.

Pelleter, J., Renaud, F., 2009. Facile, fast and safe process development of nitration and bromination reactions using continuous flow reactors. Org. Process Res. Dev. 13, 698–705. http://dx.doi.org/10.1021/op8002695.

Qian, D., Lawal, A., 2006. Numerical study on gas and liquid slugs for Taylor flow in a T-junction microchannel. Chem. Eng. Sci. 61, 7609–7625. http://dx.doi.org/10.1016/j.ces.2006.08.073.

Roudet, M., Loubiere, K., Gourdon, C., Cabassud, M., 2011. Hydrodynamic and mass transfer in inertial gas–liquid flow regimes through straight and meandering millimetric square channels. Chem. Eng. Sci. 66, 2974–2990. http://dx.doi.org/10.1016/j.ces.2011.03.045.

Shao, N., Gavriilidis, a., Angeli, P., 2010. Mass transfer during Taylor flow in microchannels with and without chemical reaction. Chem. Eng. J. 160, 873–881. http://dx.doi.org/10.1016/j.cej.2010.02.049.

Stankiewicz, A.I., Moulijn, J.a., 2000. Process intensification : transforming chemical engineering. Chem. Eng. Prog., 22–34

Théron, F., Anxionnaz-Minvielle, Z., Cabassud, M., Gourdon, C., Tochon, P., 2014. Characterization of the performances of an innovative heat-exchanger/reactor. Chem. Eng. Process. Process Intensif. 82, 30–41. http://dx.doi.org/10.1016/j.cep.2014.04.005.

Tochon, P., Couturier, R., Anxionnaz, Z., Lomel, S., Runser, H., Picard, F., Colin, A., Gourdon, C., Cabassud, M., Peerhossaini, H., Della Valle, D., Lemenand, T., 2010. Toward a competitive process intensification: a new generation of heat exchanger-reactors. Oil Gas Sci. Technol. – Rev. d'IFP Energies Nouv. 65, 785–792. http://dx.doi.org/10.2516/ogst/2010020.

Tsoligkas, A.N., Simmons, M.J.H., Wood, J., 2007. Influence of orientation upon the hydrodynamics of gas-liquid flow for square channels in monolith supports. Chem. Eng. Sci. 62, 4365–4378. http://dx.doi.org/10.1016/j.ces.2007.04.051.

van Baten, J.M., Krishna, R., 2004. CFD simulations of mass transfer from Taylor bubbles rising in circular capillaries. Chem. Eng. Sci. 59, 2535–2545. http://dx.doi.org/10.1016/j.ces.2004.03.010.

Dean, W.R., 1928. Fluid motion in a curved channel. Proc. R. Soc. London A Math. Phys. Eng. Sci. 121, 402–420.

Winkler, L.W., 1888. Die Bestimmung des im Wasser gelösten Sauerstoffes. Berichte der Dtsch. Chem. Gesellschaft 21, 2843–2854. http://dx.doi.org/10.1002/cber.188802102122.

Xiong, R., Chung, J.N., 2007. Flow characteristics of water in straight and serpentine micro-channels with miter bends. Exp. Therm. Fluid Sci. 31, 805–812. http://dx.doi.org/10.1016/j.expthermflusci.2006.08.006.

Yang, L., Dietrich, N., Hébrard, G., Loubière, K., Gourdon, C., 2016a. Optical methods to investigate the enhancement factor of an oxygen-sensitive colorimetric reaction using microreactors. AIChE J. http://dx.doi.org/10.1002/aic.15547.

Yang, L., Dietrich, N., Loubière, K., Gourdon, C., Hébrard, G., 2016b. Visualization and characterization of gas–liquid mass transfer around a Taylor bubble right after the formation stage in microreactors. Chem. Eng. Sci. 143, 364–368. http://dx.doi.org/10.1016/j.ces.2016.01.013.

Yao, C., Dong, Z., Zhao, Y., Chen, G., 2014. An online method to measure mass transfer of slug flow in a microchannel. Chem. Eng. Sci. 112, 15–24. http://dx.doi.org/10.1016/j.ces.2014.03.016.

Zuber, N., Findlay, J.A., 1965. Average volumetric concentration in two-phase flow systems. J. Heat Transf. 87, 453–468. http://dx.doi.org/10.1115/1.3689137.